machines

MDPI

Article

Multi-Objective Optimization of Gear Design of E-Axles to Improve Noise Emission and Load Distribution

Luciano Cianciotta, Marco Cirelli and Pier Paolo Valentini *

Department of Enterprise Engineering, University of Rome Tor Vergata, 00133 Rome, Italy; luciano.cianciotta@uniroma2.it (L.C.); marco.cirelli@uniroma2.it (M.C.)
* Correspondence: valentini@ing.uniroma2.it

Abstract: This paper presents a comprehensive methodology to enable the optimization of an automotive electric axle to reduce noise emissions and improve load distribution. The proposed method consists of the application of two sequential optimization procedures. The first one focuses on the gears' macro-geometry, based on an objective function that combines the contact ratio, power loss, and center distance. The second one optimizes the micro-geometry of the teeth to reduce the sound pressure generated by tooth impacts. Mechanical stress limits are considered as a constraint in the optimization process. Shafts, joints, and the electric motor are analyzed, taking into account their deformation that influences the dynamics of the entire system. The results of the proposed procedure are verified through experimental measurements and the comparison can be considered successful.

Keywords: gear design; noise; power loss; gear optimization; e-axle; automotive

Academic Editor: Walter D'Ambrogio

Received: 19 March 2025
Revised: 11 April 2025
Accepted: 15 April 2025
Published: 17 April 2025

Citation: Cianciotta, L.; Cirelli, M.; Valentini, P.P. Multi-Objective Optimization of Gear Design of E-Axles to Improve Noise Emission and Load Distribution. *Machines* **2025**, *13*, 330. https://doi.org/10.3390/machines13040330

1. Introduction

Optimizing the acoustic performance of gears has become a major challenge in the design of mechanical systems, particularly for e-axles, whose spread is being promoted by the boost towards the massive electrification in the automotive industry. The design of electric axles is a key element in the architecture of electric and hybrid vehicles, enabling the conversion of electrical energy generated by the electric machine into mechanical energy transmitted to the wheels via a gear reducer. The use of a high-ratio gear reducer is mandatory since the speed of the electric motor is significantly higher than that required by the tires. High manufacturers' standards require that the design of such a gearbox must ensure efficiency, durability, and also acoustic comfort. The acoustic optimization of gears can be addressed with different design strategies, involving combined aspects of their geometry and manufacturing: the choice of the number of teeth and their macro-geometry [1]; tooth profile corrections (micro-geometry) that alter the shape with respect to the involute profile [2]; and the control of the surface finishing and manufacturing tolerances [3,4]. Each element may contribute to improving the overall acoustic performance.

The optimization of macro-geometry, which concerns the choice of tooth number, pressure and helix angle, module, profile shift, and backlash, directly influences the acoustic emission during meshing. This is strictly related to the contact ratio, which measures the number of teeth in contact simultaneously between two gears during their meshing. Studies by Kahraman et al. [5] have shown experimentally the effect of contact ratio on the torsional vibrations of a spur gear pair with the assessment of the dynamic transmission error and contact forces. In addition, T. Sato et al. [6] analyzed the effect of vibration in a large set of contact ratios using simulations and experimental data. He demonstrated that optimization

depends on the profile correction adopted and that, as the contact ratio increases, vibration tends to decrease. However, increasing contact ratio requires teeth with a smaller pressure angle, reduced pitch, or extended addendum. All factors affect tooth stress, possible interference, high wear and also pitting risk [7–9]. Therefore, the acoustic optimization depends on a combination of parameters and aims to find an adequate trade-off between reliability, efficiency, and noise emission.

Tooth profile optimization (micro-geometry) is related to the ability to compensate for tooth deflection during meshing due to high loads and misalignment. Tooth bending, gear body distortions, and whole gear body give an overall relative deflection at the contact point that produces a displacement from the ideal angular position of the gears. This effect is measured through the transmission error (TE), defined as the difference between the actual position of the driven gear and what it would be in the case of ideal kinematic meshing [10]. The TE can be evaluated in static and dynamic conditions using analytical and numerical approaches [11,12]. Moreover, several novel approaches have been introduced to evaluate the TE in dynamic conditions, using multibody dynamic simulations as a valid tradeoff between accuracy and computational efficiency [13]. Since the TE directly influences the vibration of the gearing system, efforts have been made by the scientific community to reduce the amplitude of the TE. Profile modification is one of the most common solutions to reduce the TE. For this reason, several methods are present in the literature regarding the effects of the profile modification on the dynamic response of the gear system [14–16].

Other studies [17,18] have also focused on the different techniques for measuring TE and correlating it with the dynamic factor [19]. A good practice in the design phase is to apply a modification to the profile in order to ensure a more uniform load distribution to minimize contact stresses, friction forces [20,21], and tooth wear, and reduce power loss [22,23]. Another element that affects the acoustic emission is the tooth surface roughness due to sliding [24,25]. Different researchers have shown that gear machining may be one way to control acoustic emissions and vibration transmission. Experiments conducted on a pair of bevel gears [26] show that using different manufacturing techniques (lapping process, hard finishing process), it is possible to reduce the amplitude of meshing harmonics, improving noise emission and reducing pitch.

Several multi-objective processes are proposed in the literature to reduce whine noise, improve efficiency, and minimize transmission errors in gear design. One approach uses the Non-Dominated Sorting Genetic Algorithm II (NSGA-II) to optimize both macro- and micro-geometry parameters of a gear unit, aiming to minimize power loss and vibrational excitation, emphasizing the importance of simultaneous optimization of these factors [27]. Another study focuses on agricultural tractors, where gear macro-geometry is optimized using the Non-Dominated Sorting Genetic Algorithm III (NSGA-III) to reduce transmission gear whine noise, leading to a 3.1 dBA reduction in noise levels and improved comfort for the driver [28]. The optimization of helical gear macro-geometry to achieve low weight, high efficiency, and reduced noise is also explored, with a focus on the trade-off among these objectives [29]. Furthermore, the influence of gear tooth addendum and dedendum on optimization results has been investigated, showing improvements when these parameters are considered alongside other design variables [30]. In another work, the response surface methodology is applied for micro-geometry optimization, significantly reducing peak-to-peak transmission errors and contact stress while maintaining the required safety coefficient [31]. A robust methodology for optimizing both macro- and micro-geometry, focusing on minimizing static transmission error and mesh stiffness fluctuations, is introduced, with Monte Carlo simulations used to account for manufacturing errors [32]. Another structured approach combines meta-models and robust optimization to improve gear microgeometry, yielding gains in transmission error reduction and stress

minimization [33]. Recent research also investigates the optimization of gear design using a multi-objective approach to find the best way to achieve minimum dynamic excitation, including gear-mesh stiffness and dynamic behavior as objective functions [34]. Finally, robust optimization techniques based on contact ratio control are used to address the effects of mounting errors on helical gears, improving performance under different torque conditions [35].

Several studies in the literature address the optimization of transmission noise vibration harshness (NVH) performance, with a focus on the minimization of the transmission error even to design spur gears considering multiple failure modes [36]. However, it is often observed that NVH-optimal solutions can negatively impact reliability, particularly as the contact ratio increases. Moreover, tooth profile optimization is performed not only to reduce transmission error but also to ensure centered tooth contact in the presence of misalignments caused by shaft and housing deflections. Unlike other scientific studies, the optimization of acoustic performance is carried out considering all aspects of the transmission such as reliability, efficiency, center distance, stress distribution along tooth width, and specific sliding. Another difference is the use of the approach to optimize NVH performances. Many studies have explored minimizing the transmission error, while in this work, we used a simplified sound pressure model proposed by Masuda [37], which considers not only transmission error but also macro-geometric aspects of the gears, such as contact ratio, helix angle, transmission ratio, tangential speed, and transmitted power.

From the analysis of scientific literature, it is clear that a complete NVH design of an e-axle needs to include both aspects related to the macro-geometry of the gears and aspects related to their micro-geometry. In addition, since the actual loads exchanged by the gears as well as the vibration phenomena are influenced by the compliance of support structures such as bearing and shafts, they must necessarily be included in all design evaluations. Dealing with an optimization that includes all these aspects simultaneously can be computationally burdensome and not suitable for quickly evaluating different design alternatives. Hence, the idea of the present work was to approach the design of an e-axle through a procedure consisting of two steps that implement two successive optimizations.

- First step: macro-geometry optimization, based on an objective function that combines the contact ratio—closely related to sound pressure—with dissipated power and the center distance between shafts. To reduce the computational cost and explore a larger number of solutions, transmission error and, consequently, sound pressure are not computed at this stage. Only gear parameters are considered without shafts and their deflection.
- Second step: micro-geometry optimization, performed using sound pressure as the cost function, incorporating tooth contact analysis and transmission error calculation. Stress distribution is considered a constraint in the optimization process. Shafts, joints, and electric motors are considered with their structural behavior.

The proposed methodology is based on a lumped-parameter model of the entire transmission in order to take into account all the relevant contributions. The procedure is described using a specific implementation of an e-axle, thus being able to address the various steps in detail. However, none of the assumptions or initial hypotheses confine the proposed methodology to the selected case, keeping it completely general for a much wider application in the automotive field.

The novel contribution of this work is the introduction of a multi-objective optimization approach that integrates various design criteria to achieve the best gear design on multiple aspects such as noise emission, power loss, and size. Unlike conventional methods that typically focus on isolated aspects—such as minimizing noise or maximizing strength—this method aims to optimize the entire transmission architecture by simultane-

ously reducing acoustic emissions and meshing losses. A distinctive feature of the approach is its ability to address both macro- and micro-geometrical parameters within a unified optimization framework. This is particularly relevant given the complex trade-offs involved, as design variables often exert opposing effects on performance targets. The effectiveness of the proposed method is demonstrated through a case study, whose outcomes are validated against experimental data.

The paper is organized as follows. The first part describes modeling of the main e-axle components. Then, the two-step optimization procedure is introduced focusing on both macro- and micro-geometrical steps. In the third part, the case study is introduced, and in the last part, the results of numerical optimizations are compared to those from experimental campaigns.

2. E-Axle Modeling Approach and Subcomponents

In very general terms, an automotive e-axle is a mechanical transmission system that combines the presence of some main elements including electric motors, connecting shafts, bearings, and gears. In order to describe the structural behavior of these elements, it is necessary for each of them to deduce a mathematical model that is reliable and computationally efficient. It was decided to model each of these functional blocks by means of a lumped-parameter approach that allows the main characteristics to be taken into account without having to struggle with a detailed discretization. Each block is defined with its inputs and outputs in order to be connected with adjacent blocks using sequential logic to easily compose even complex embodiments. The modeling details of each block are presented below.

2.1. Electric Motor

The electric motor is modeled as a driving element (Figure 1), incorporating the torque-speed map that defines the operational characteristics of the component. Using the rotational speed of the electric machine as the input, the transmitted torque is obtained as the output (the nomenclature of the parameters is reported in Table 1). Dynamic effects such as torque ripple, radial and tangential forces, and frictional forces are excluded from the model, as its purpose is not to analyze housing vibrations but rather to evaluate the acoustic emissions of the gears and the forces transmitted through the meshing process.

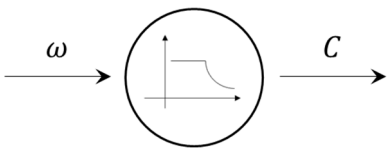

Figure 1. Electric motor model input/output.

Table 1. Input/output data for electric motor.

Input			**Output**		
Speed	ω	[rpm]	Torque	C	[Nm]

2.2. Ball Bearings

The ball bearings are modeled as elastic elements (Figure 2). In the case of ball bearings, they connect the ground to the respective shaft, whereas roller bearings provide a connection between two bodies.

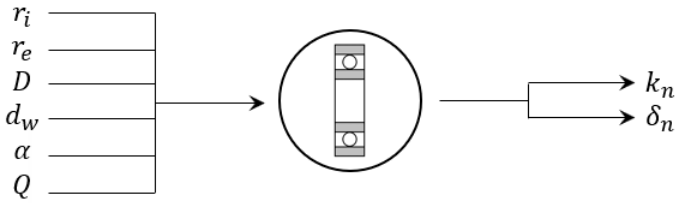

Figure 2. Bearings model input/output.

In Table 2, all the referenced parameters are summarized.

Table 2. Input/output data for bearing model.

Input			Output		
Internal raceway groove curvature radius	r_i	[mm]	Stiffness	k_n	[N/m]
External raceway groove curvature radius	r_e	[mm]	Deflection	δ_n	[mm]
Ball diameter	D	[mm]			
Bearing pitch diameter	d_w	[mm]			
Contact angle	α	[°]			
Normal load	Q	[N]			

The stiffness of the bearings is calculated based on Hertzian contact theory and with the use of standard ISO 16281 [38]. Under a normal load, the contact area between the ball and the inner and outer raceways is elliptical, as shown in Figure 3. The contact pressure distribution takes the shape of a paraboloid. The normal load can be related to the contact deformation according to the following formulation:

$$Q = k\delta^{3/2} \tag{1}$$

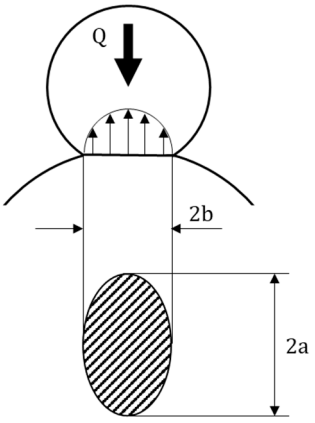

Figure 3. Contact model of the ball and grooves inside the bearing.

The curvature parameters for the inner and outer raceways are calculated. The elongation ratio χ of the ellipse and the equivalent curvature Γ are defined as

$$\chi = \frac{a}{b} \tag{2}$$

$$\Gamma = \frac{1}{R_1} + \frac{1}{R_2} \tag{3}$$

$$\gamma = \frac{D\cos\alpha}{d_m} \tag{4}$$

that for the inner raceway becomes

$$R_x = (1-\gamma)\cdot\frac{D}{2} \tag{5}$$

$$R_y = \frac{r_i}{\frac{2r_i}{D}-1} \tag{6}$$

while for outer raceway becomes

$$R_{xe} = (1+\gamma)\cdot\frac{D}{2} \tag{7}$$

$$R_{ye} = \frac{r_e}{\frac{2r_e}{D}-1} \tag{8}$$

The elongation ratio χ is obtained by solving the following equation:

$$1-\frac{2}{\chi^2-1}\left(\frac{F(\chi)}{S(\chi)}-1\right)-\Gamma=0 \tag{9}$$

where $F(\chi)$ and $S(\chi)$ are the elliptic integrals of the first and second kind, respectively:

$$F(\chi)=\int_0^{\pi/2}\frac{1}{\sqrt{1-\left(1-\frac{1}{\chi^2}\right)\sin^2\psi}}d\psi \tag{10}$$

$$S(\chi)=\int_0^{\pi/2}\sqrt{1-\left(1-\frac{1}{\chi^2}\right)\sin^2\psi}d\psi \tag{11}$$

The integrals can be solved numerically, as no analytical solution exists. At this point, the contact stiffness for the individual interaction between the ball and each raceway can be calculated:

$$k=\frac{\sqrt{2}}{3}\cdot\frac{\pi E}{1-\nu^2}\cdot\chi^2\sqrt{\frac{2F(\chi)}{\Gamma S(\chi)^3}} \tag{12}$$

Considering the deformation with the outer raceway δ_e and the inner raceway δ_i we have

$$Q=k_e\delta_e^{3/2}=k_i\delta_i^{3/2} \tag{13}$$

The total deformation δ_n and the total stiffness k_n are calculated accordingly:

$$\delta_n=\delta_i+\delta_e \tag{14}$$

$$k_n=\left(\frac{1}{k_i^{2/3}}+\frac{1}{k_e^{2/3}}\right)^{3/2} \tag{15}$$

2.3. Shafts

The shafts are modeled using the elastic theory of the Euler beam model under the hypothesis of small displacements. Figure 4 shows the input and output parameters of the shaft model.

In Table 3, all the input and output parameters for the shaft model are summarized.

To calculate the shaft deflection, the following data are required:

- Shaft geometry: The shaft is divided into n sections, each characterized by its length L, inner diameter D_i, and outer diameter D_e;

- Material properties: Young's modulus E, shear modulus G, moment of inertia I, polar moment of inertia J, and cross-sectional area A;
- Boundary conditions: types of constraints, such as hinges, fixed supports, and bearings;
- Applied loads: radial and axial forces, as well as torques, including forces generated by gears or pulleys.

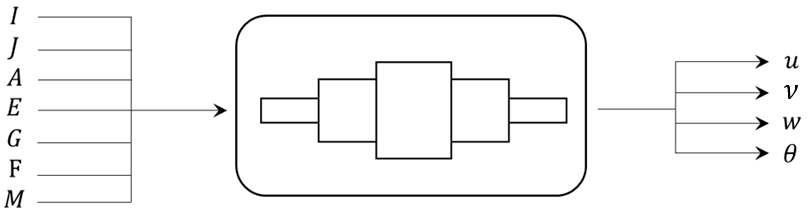

Figure 4. Elastic shaft model input and output parameters.

Table 3. Input and output parameters for the shaft model.

Input			Output		
Moment of inertia	I	[mm^4]	Axial displacement	u	[mm]
Polar moment of inertia	J	[mm^4]	Vertical displacement	v	[mm]
Area	A	[mm^2]	Transverse displacement	w	[mm]
Young modulus	E	[N/mm^2]	Torsion angle	θ	[°]
Shear modulus	G	[°]			
Applied torque	M	[Nmm]			

Given the external forces F_e and torques M_e applied to the shaft, the reaction forces F_i and reaction moments M_i at the supports (e.g., bearings, joints, or other constraints) are calculated using the following equilibrium equations:

$$\sum \vec{F}_i = \sum \vec{F}_e \tag{16}$$

$$\sum \vec{M}_i = \sum \vec{M}_e \tag{17}$$

Each segment (each portion with the same cross-section) is treated as a beam, with the elastic equations solved separately and then connected through continuity conditions at the boundaries (displacement and slope). Depending on the type of deformation to be determined, whether the vertical displacement v, transverse displacement w, axial displacement u, or torsion angle θ, the following differential equations are solved:

- Bending

$$M_z(x) = EI_{xx}\frac{d^2v(x)}{dx^2},\ M_y(x) = EI_{yy}\frac{d^2w(x)}{dx^2} \tag{18}$$

$$F_y(x) = EI_{xx}\frac{d^3v(x)}{dx^3},\ F_z(x) = EI_{yy}\frac{d^3w(x)}{dx^3} \tag{19}$$

- Torsion

$$M_z(x) = GJ\frac{d\theta_z}{dx} \tag{20}$$

- Stretching

$$F_x(x) = EA\frac{du}{dx} \tag{21}$$

The next step is to apply the continuity conditions between elements. For instance, in the case of bending for a single *i*-th segment, the elastic equation is integrated twice:

$$\frac{dv}{dx} = \int \frac{M(x)}{E_i I_i} dx + C_{1i} \tag{22}$$

$$v(x) = \int \left(\int \frac{M(x)}{E_i I_i} dx \right) dx + C_{1i} x + C_{2i} \tag{23}$$

where C_{1i} and C_{2i} are the integration constants that are specific to each segment. The continuity conditions between *i*-th and $(i + 1)$-th elements impose the following:

- The deflection $v(x)$ must be continuous at every connection point between two segments at the junction x_c. The following equation is enforced:

$$v_i(x_c) = v_{i+1}(x_c) \tag{24}$$

- The slope $dv(x)/dx$ must be continuous at transition points, except in the presence of discontinuities in the bending moment (e.g., applied torques):

$$\frac{dv_i(x_c)}{dx} = \frac{dv_{i+1}(x_c)}{dx} \tag{25}$$

The boundary conditions depend on the type of constraints on the shaft. The constants C_{1i} and C_{2i} are determined by enforcing these conditions at the constraint points and solving the resulting system.

2.4. Gears

Gear elements are modeled by including both the macro-geometry and the profile modifications applied to the teeth. In Figure 5, all the parameters of the model are summarized and then reported with their units in Table 4. The detailed description of the micro- and macro-geometric parameters are reported in Sections 5 and 6, respectively.

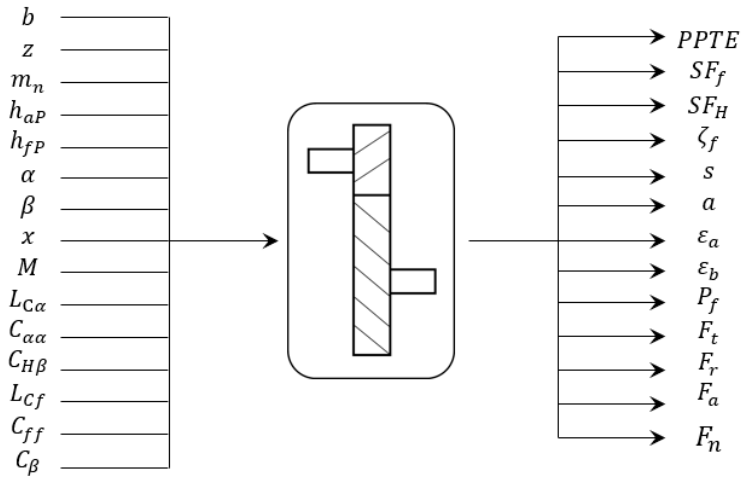

Figure 5. Gear model input/output.

For the calculation of the shaft deformation and the bearing reactions, the meshing forces are firstly evaluated (radial, axial, and tangential forces):

- Tangential force:

$$F_t = \frac{2M}{d_p} \tag{26}$$

- Radial force:

$$F_r = F_t \cdot \tan \alpha_t \tag{27}$$

- Axial force:

$$F_a = F_t \cdot \tan \beta \tag{28}$$

- Normal force:

$$F_n = \sqrt{F_t^2 + F_r^2 + F_a^2} \tag{29}$$

where

$$\alpha_t = \operatorname{atan}\left(\frac{\tan \alpha_n}{\tan \beta}\right) \tag{30}$$

Table 4. Input/output data for gear model.

Input			Output		
Face width	b	[mm]	Peak–peak static transmission error	$PPTE$	[µm]
Number of teeth	z	[-]	Tooth bending strength	SF	[-]
Normal module	m_n	[mm]	Tooth pitting resistance	SH	[-]
Addendum	h_{aP}	[mm]	Specific sliding	ζ_f	[°]
Dedendum	h_{fP}	[mm]	Center distance	a	[mm]
Pressure angle	α	[°]	Transverse contact ratio	ε_a	[-]
Helix angle	β	[°]	Axial contact ratio	ε_b	[-]
Correction factor	x	[-]	Total power loss	P_V	[kW]
Torque	M	[Nm]	Tangential force	F_t	[N]
Tip relief length	$L_{C\alpha}$	[µm]	Radial force	F_r	[N]
Tip relief amplitude	$C_{\alpha\alpha}$	[µm]	Axial force	F_a	[N]
Flank line slope modification	$C_{H\beta}$	[µm]	Normal force	F_n	[N]
Root relief length	L_{Cf}	[µm]			
Root relief amplitude	C_{ff}	[µm]			
Flank line crowning	C_β	[µm]			

Once the shaft deformation and the displacement of the wheel body have been calculated, the transmission error is determined. To calculate the static transmission error (STE), the flexibility of the tooth must be considered. The tooth stiffness is modeled according to the theory of Weber [39], which considers three effects:

- Gear body deformation (see Figure 6 for the meaning of the parameters)

$$\delta_{t_i} = \frac{F_t}{b}\cos^2(\alpha_t)\frac{1-\nu^2}{E}\left[\frac{18y_p^2}{\pi s_p^2} + \frac{2(1-2\nu)}{1-\nu}\frac{y_p}{s_p} + \frac{4.8}{\pi}\cdot\left(1 + \frac{1-\nu}{2.4}\tan^2(\alpha_t)\right)\right] \tag{31}$$

- Tooth bending deformation (see Figure 7 for the meaning of the parameters)

$$\delta_{b_i} = \frac{F_t}{b}\cos^2(\alpha_t)\frac{1-\nu^2}{E}\left[12\int_0^{y_p}\frac{(y_p-y)^2}{(2x')^3}dy + \left(\tan^2(\alpha_t) + \frac{2.4}{1-\nu}\right)\int_0^{y_p}\frac{dy}{2x'}\right] \tag{32}$$

- Contact deformation (see Figure 8 for the meaning of the parameters)

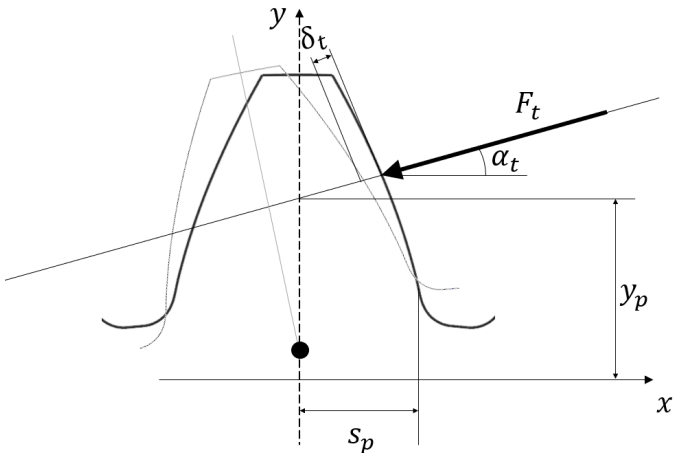

Figure 6. Gear body deformation.

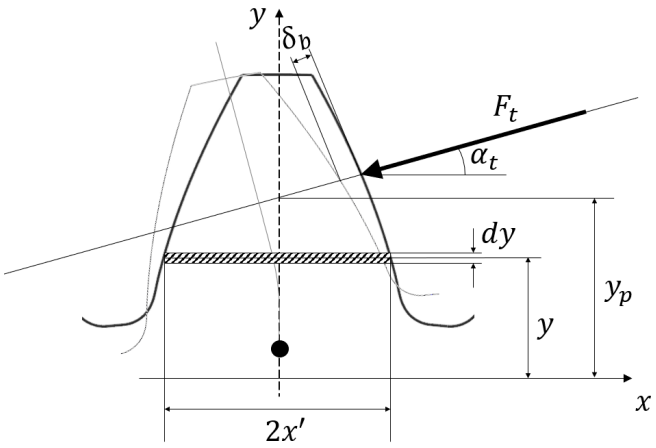

Figure 7. Tooth bending deflection.

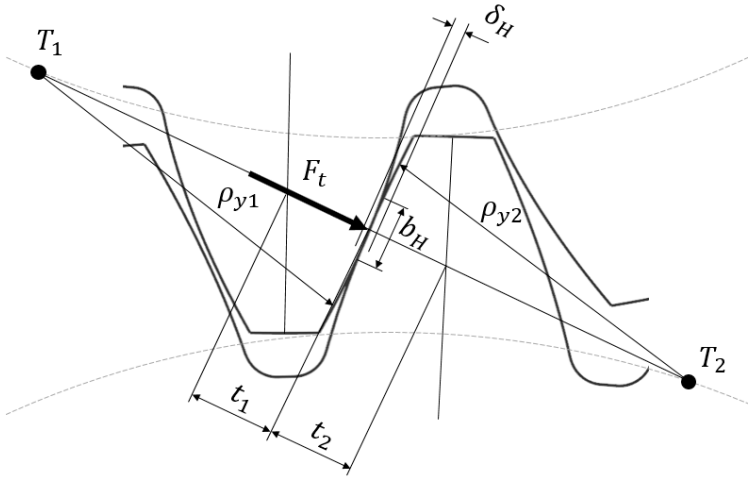

Figure 8. Contact deformation during tooth meshing.

$$\delta_{H_{1,2}} = \frac{F_t}{\pi b}\left(\left|\frac{1-\nu_1^2}{E_1}\ln\left(\frac{b_H^2}{4t_1^2}\right)+\frac{\nu_1(1+\nu_1)}{E_1}\right|+\left|\frac{1-\nu_2^2}{E_2}\ln\left(\frac{b_H^2}{4t_2^2}\right)+\frac{\nu_2(1+\nu_2)}{E_2}\right|\right) \quad (33)$$

$$b_H = \sqrt{\frac{4}{\pi}F_t\frac{\rho_{y_1}\cdot\rho_{y_2}}{\rho_{y_1}+\rho_{y_2}}\left(\frac{1-\nu_1^2}{E_1}+\frac{1-\nu_2^2}{E_2}\right)} \quad (34)$$

Therefore, the transmission error calculated along the path of contact is

$$STE = \delta_{t_1} + \delta_{b_1} + \delta_{H_{1,2}} + \delta_{t_2} + \delta_{b_2} \tag{35}$$

The tooth stiffness, in the case of cylindrical gears, is given by

$$C = \frac{F_t}{STE} \tag{36}$$

It is interesting to notice that, even if at this stage the model does not account for lightning features or the presence of holes in the gear body, these features can be introduced by modifying the mesh stiffness related to the rim and modifying the inertia properties of the gears accordingly.

The model is extended to the case of helical gears. In particular, the approach proposed in the literature [40] is used, where the gear is divided into multiple infinitesimal slices connected by a torsional spring with stiffness C_c:

$$C_c = f \cdot A_{sec}^2 \cdot \frac{C_i + C_{i+1}}{2} \tag{37}$$

where A_{sec} is the number of slices and f is the slices linking factor, with a typical value of 0.04 [40]. C_i and C_{i+1} are the total stiffnesses of the i-th tooth and $(i+1)$-th slice, respectively. The set of equations that describe the force–displacement relationship is given by

$$\begin{bmatrix} C_1 + C_c & -C_c & 0 & 0 & \cdots & 0 \\ -C_c & C_2 + 2C_c & -C_c & 0 & \cdots & 0 \\ 0 & -C_c & C_3 + 2C_c & -C_c & 0 & \vdots \\ 0 & 0 & -C_c & \ddots & -C_c & 0 \\ \vdots & \vdots & 0 & -C_c & C_{n-1} + 2C_c & -C_c \\ 0 & 0 & \cdots & 0 & -C_c & C_n + C_c \end{bmatrix} \begin{Bmatrix} \delta_1 \\ \delta_2 \\ \delta_3 \\ \delta_4 \\ \vdots \\ \delta_n \end{Bmatrix} = \begin{Bmatrix} F_{t1} \\ F_{t2} \\ F_{t3} \\ F_{t4} \\ \vdots \\ F_{tn} \end{Bmatrix} \tag{38}$$

The specific sliding ζ_f can be defined as the ratio between the sliding velocity of the pinion, $v_{\rho 1}$, and that of the gear, $v_{\rho 2}$. It refers to the gear (2) and pinon (2) as the ratio to the respective sliding velocity. Let us consider ζ_{f_1}

$$\begin{aligned} \zeta_{f_1} &= \frac{v_{\rho 1} - v_{\rho 2}}{v_{\rho 1}} \\ \zeta_{f_2} &= \frac{v_{\rho 1} - v_{\rho 2}}{v_{\rho 2}} \end{aligned} \tag{39}$$

The pitting verification for gears is a fundamental analysis to evaluate the resistance of tooth surfaces to cyclic loading. This procedure helps to prevent the formation of microcracks and progressive wear phenomena, thereby ensuring the durability, reliability, and efficiency of the transmission system. Pitting verification involves the assessment of the contact stress caused by the applied loads, denoted as σ_H, and comparing it with the allowable limit, σ_{HG}, under operating conditions. The detailed procedure to compute these terms is explained in [41] and reported in the Appendix A.1 for completeness.

Moreover, in order to include into the optimization the root stress limit σ_F, the tooth root stress limit σ_{FG}, and the bending safety factor S_F, the procedure proposed in the ISO standard [42] is also considered. The detailed procedure is reported in Appendix A.2 for completeness.

When the power is transmitted through a gear unit, various components experience losses that generate heat. The total power losses (P_V) in a gear unit comprise load-

dependent losses and zero-load contributions. According to ISO/TR 1419-2 [43], the overall power loss of a transmission can be evaluated as

$$P_V = P_{VZ0} + P_{VZP} + P_{VL0} + P_{VLP} + P_{VD} + P_{VX} \tag{40}$$

where P_{VZ0} is the zero-load-dependent loss derived by churning/windage/squeezing, P_{VZ} is the load-dependent loss associated with tooth friction, P_{VL0} the load-independent loss of roller bearings, P_{VLP} is the load-dependent loss of roller bearings, P_{VD} is the loss due to seals, and P_{VX} incorporates all the other auxiliary losses not included in the previous components. The detailed procedure to compute these terms is explained in [43] and reported in the Appendix A.3 for completeness.

3. Noise Prediction Model

The semi-empirical equation developed by Masuda provides a practical approach for estimating gear noise at 1 m [22]. This method uses parameters such as transmitted power, rotational speed, contact ratio, gear ratio, helix angle, and accuracy grade. The following equation demonstrates strong alignment with experimental results under standard operating conditions. The Masuda formulation is used to compare different gear geometries with the hypothesis that the gears are changed in the gearbox used to validate the semi-empirical equation. So is it possible to estimate the sound pressure level (SPL) for meshing:

$$\begin{aligned} SPL = {} & \frac{20\cdot\left(1-\tan\left(\frac{\beta}{2}\right)\right)\cdot\tau^{0.125}}{\varepsilon_\alpha^{0.25}}\cdot\sqrt{\frac{5.56+\sqrt{v}}{5.56}} + 20\cdot\log_{10}(W) + \\ & + 20\cdot\log_{10}\left(\frac{PPTE}{F_n}\cdot b\cdot C\right) + 20 \end{aligned} \tag{41}$$

where

β is the helix angle;
τ is the transmission ratio;
ε_α is the transverse contact ratio;
v is the tangential velocity;
W is the input power;
$PPTE$ is the peak-to-peak static transmission error;
F_n is the normal tooth force;
l is the effective face width;
C is the mean mesh stiffness.

Equation (41) is closely related to the geometric characteristics of the transmission, particularly the number of teeth, helix, and pressure angles, as well as the center distance, height, and thickness of the teeth. This term plays a predominant role as the operating speed of transmission increases. It highlights that an increase in the contact ratio can contribute to reducing noise emissions. Two significant challenges should be carefully addressed. First, achieving high contact ratio (HCR) features in spur gears involves increasing the addendum coefficient or decreasing the normal pressure angle. While increasing the addendum coefficient results in higher relative sliding velocities and necessitates a larger minimum tooth count to prevent undercutting, decreasing the normal pressure angle compromises the bending strength of the gears. Second, unavoidable elastic deformations and machining inaccuracies lead to interference or separation between meshing teeth. This issue is particularly pronounced in HCR gear transmissions, where the simultaneous engagement of multiple teeth amplifies noise and reduces efficiency. Therefore, it is essential to properly size the gears, identifying the optimal combination of parameters to maximize the contact ratio, while preserving structural reliability and minimizing power losses. The second term of the equation is linked to the transmitted power, a constant independent of

the geometric configuration of the gears. The third term is associated with the flexibility of the teeth and force variations that may occur during operations. The variation in transmission error over a meshing cycle is directly influenced by the tooth profile. The choice of micro-geometry represents a complex challenge, as it affects both noise emissions and the tooth's ability to compensate for misalignments caused by assembly tolerances and the flexibility of shafts and housings.

The use of a simplified formulation such as that of Masuda allows us to identify promising configurations without the computational complexity of high-fidelity acoustic simulations, which are more appropriate in the final stages of the design process. It is important to note that Masuda's approach does not account for factors such as the actual stiffness and geometry of the housing, wave propagation and reflection phenomena, or dynamic effects like resonances. Nonetheless, in the early stages of the design process, the availability of a comparative and computationally efficient procedure capable of providing insight into optimal configurations is of significant industrial relevance, as it enables rapid exploration of the design space and early identification of viable design directions.

For high-performance transmission applications, it is crucial to identify a configuration that not only maximizes performance but also ensures reduced weight and high efficiency. In the early stages of design, it is advisable to explore unconventional solutions and define design guidelines for the components. To this end, optimization processes serve as a fundamental support, allowing the analysis of numerous solutions that would be unmanageable using traditional iterative approaches. While the model focuses on noise generated by a single gear meshing, in systems with multiple gear meshes, noise levels are typically approximated by summing the contribution of individual meshing. However, this approach oversimplifies the physics, as the interaction of sound waves is influenced by their frequency and phase rather than being a simple additive process. For two pairs of gears in meshing we have

$$SPL = 20 \cdot \log_{10}\left(10^{\frac{SPL_1}{20}} + 10^{\frac{SPL_2}{20}}\right) \tag{42}$$

4. Optimization Strategy

As briefly described in the introduction, the optimization strategy to maximize the acoustic performance of the transmission while ensuring its reliability follows a two-step scheme. First, optimization is performed to find the macro-geometric parameters of the gears, and then the optimization moves to search for the optimal micro-geometric parameters. Therefore, the whole optimization process is divided into two steps:

(1) **Macro-geometry optimization:** This phase focuses on identifying a gear configuration that maximizes the contact ratio without compromising structural reliability. The analysis is limited to the gear pair to identify the optimal geometric configuration. Additionally, as this procedure is applied during the design setup phase, it aims to select a configuration that minimizes the center distance, thereby reducing the transmission's size and friction losses.

(2) **Micro-geometry optimization**: This phase aims to minimize the peak-to-peak transmission error (PPTE). The analysis requires a detailed study of tooth contact, including the evaluation of shaft deflection and support stiffness, which vary with the applied load. Since the load is inherently nonlinear and iterative, optimizing the macro-geometry first reduces the overall computational complexity before addressing micro-geometry.

As a final step of optimization, it is possible to introduce a cross-check verification to verify that the sequential approach has maintained the fulfillment of the structural constraints on the allowable stresses.

To limit the computational burden, optimization involves several simplifications, including the adoption of a static calculation to determine the transmission error. This approach initially disregards amplification phenomena in the transmission and shafts, deferring these aspects to subsequent detailed analysis. Both the optimization steps are performed using the non-dominated sorting genetic algorithm II NSGA-II, introduced by Deb et al. [44] due to its proven efficiency in balancing solution diversity and convergence toward the Pareto front. This algorithm has demonstrated particular effectiveness in addressing complex engineering problems, ensuring robust and versatile solutions. The algorithm is structured according to a flowchart that summarizes the main key steps, as reported in Figure 9. The algorithm is well known in the scientific community; therefore, it is not considered necessary to go into detail about each of the key points, but the interested reader can find all the details in the seminal paper of the method [44].

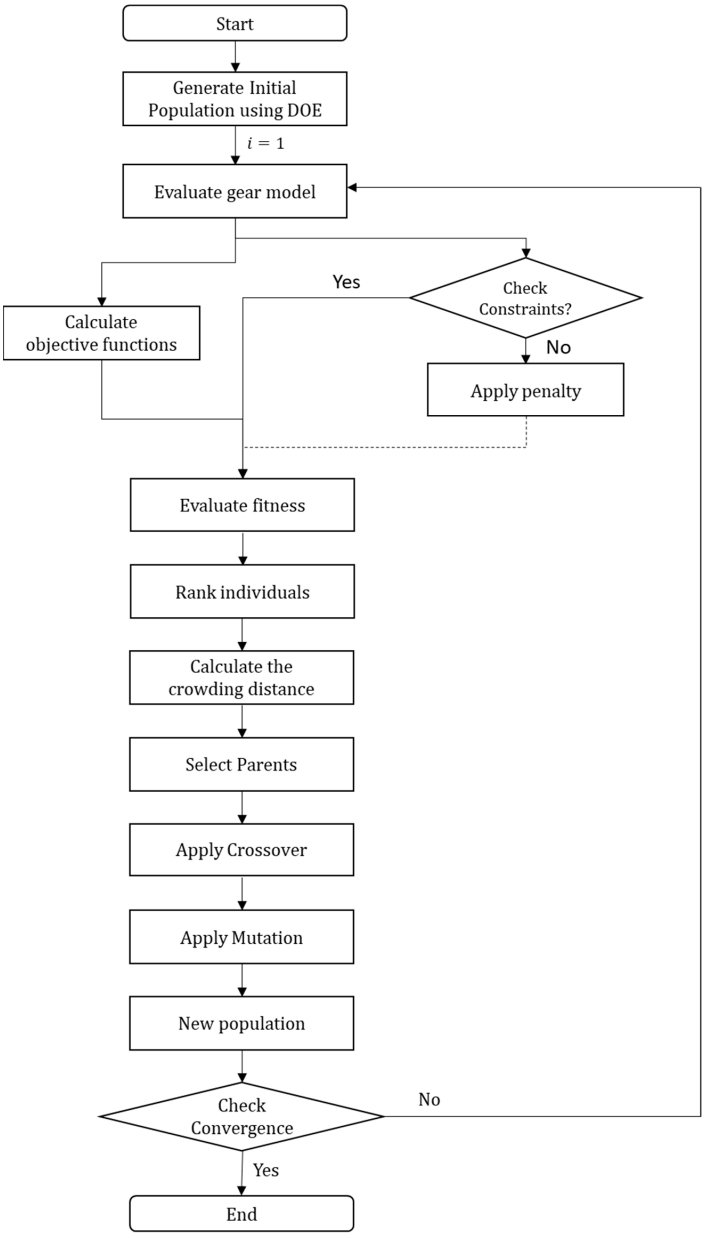

Figure 9. Flowchart of non-dominated sorting genetic algorithm II used for both the optimization steps.

5. Macro-Geometry Optimization Step

In Table 5, all the parameters used for the first step of the optimization process are described, while in Figure 10, the macro-geometry optimization variables are depicted in a drawing for a more intuitive definition. The center distance has been included among the optimization parameters because it can influence mesh stiffness, which is directly related to acoustic emission. As demonstrated by Skrickij and Bogdevičius in [45] and then Luo et al. in [46], variations in center distance can affect the dynamic behavior of the gearbox, influencing both mesh stiffness and acoustic performance. In this conceptual example, the optimizer is intended for the early stage of the design process, where positional constraints are not yet fully defined.

Table 5. Variables in the macro-geometry optimization.

Input	Optimization Variables	Constraints	Objective Functions
Electric machine power W Overall transmission ratio τ	Normal module m_n Pressure angle α Helix angle β Addendum factor h_{aP} Dedendum factor h_{fP} Number of teeth z Correction factor x Face width b	Tooth bending strength $SF_f \geq 1.5$ Tooth pitting resistance $SF_H \geq 1.5$ Specific sliding $\zeta_f \leq 3$	Center-to-center distance a Transverse contact ratio ε_a Total power loss P_V

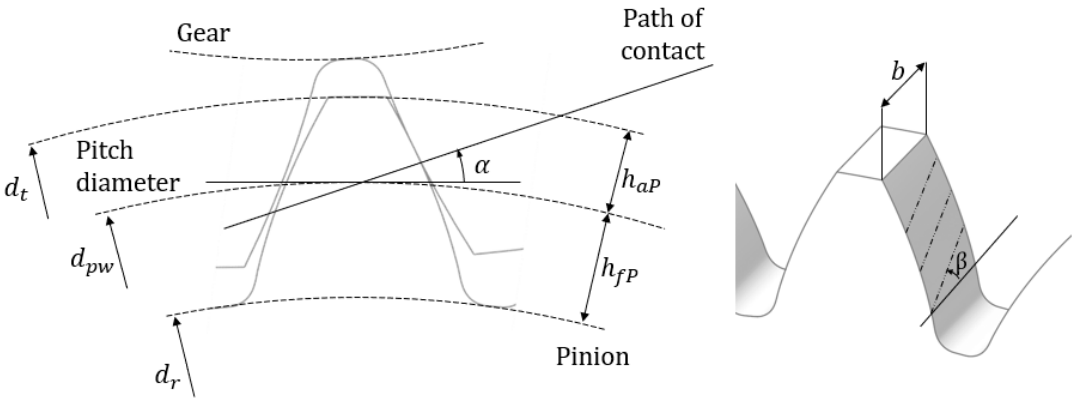

Figure 10. Variables in the macro-geometry optimization.

In this optimization process, the center line angle was not included among the design parameters. This decision is driven by the fact that, in real applications, the transmission layout is often predefined and constrained by packaging limitations and the presence of surrounding components.

The cost function to be maximized is defined as

$$F_{\text{cost}} = \frac{\varepsilon_{a_1} + \varepsilon_{a_2}}{\varepsilon_a^{\text{ref}}} - \frac{a_1 + a_2}{a^{\text{ref}}} - \frac{P_{V_1} + P_{V_2}}{P_V^{\text{ref}}} \tag{43}$$

where ε_a^{ref}, a^{ref}, and P_V^{ref} are the reference values of an initial geometry used to make the output parameters dimensionless. The negative sign is used for center–center distance and power loss because the objective is to find the best solution with maximum transverse ratio and minimum size and power loss.

The objective function is defined to minimize acoustic emissions by maximizing the contact ratio. To prevent potential trade-offs—such as reduced mechanical reliability due to

excessively thin gear teeth—appropriate optimization constraints are introduced. In cases where the optimizer tends toward thinner teeth to reduce noise, the inclusion of face width as a design variable ensures that reliability requirements are still met through the adoption of wider (and typically heavier) gears.

In Figure 11, all the parameters involved in the optimization process are shown in a flowchart scheme. The process takes as the input the transmitted power and the overall transmission ratio. The chosen cost function includes the contact ratio, related to acoustic emissions, center distance, and dissipated power. The optimization goal is to identify the gear configuration that minimizes acoustic emissions, size, and dissipated power.

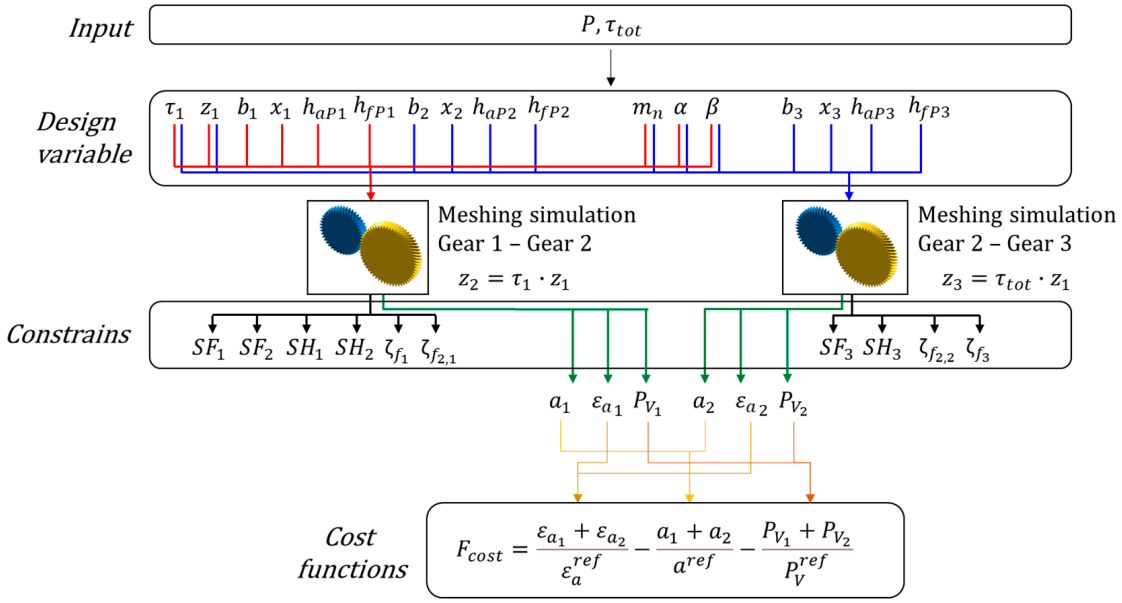

Figure 11. Flowchart of the macro-geometry optimization process.

6. Micro-Geometry Optimization Step

Once the macro-geometry optimization has been concluded, the optimization of the tooth profile is carried out. The input parameters for the second optimization step (Table 6) include the transmission ratio of each gear pair, pressure angles, helix angles, and the complete tooth geometry from the results of the previous optimization step. The optimization variables of the process are graphically reported in Figure 12.

Table 6. Variables in the micro-geometry optimization.

Input	Optimization Variables	Constraints	Objective Functions
Electric machine power, W Overall transmission ratio, τ Normal module, m_n Pressure angle, α Helix angle, β Addendum factor, h_{aP} Dedendum factor, h_{fP} Number of teeth, z Correction factor, x Face width, b	Tip relief length, $L_{C\alpha}$ Tip relief amplitude, $C_{\alpha\alpha}$ Flank line crowning, C_β Root relief length, L_{Cf} Root relief amplitude, C_{ff} Flank line slope modification, $C_{H\beta}$	Face load factor, $K_{H\beta} \geq 1.1$	Peak—peak of STE, $PPTE$ Sound pressure level, SPL

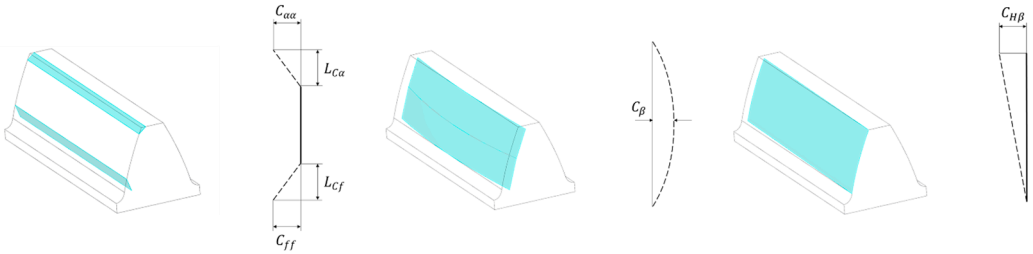

Figure 12. Optimization variables in micro-geometry step. On the left: tip and root reliefs; in the middle: lead crowning; on the right: flank line slope modification.

The micro-geometry of the gears is optimized to minimize noise emissions, which, as previously described, are assessed using Masuda's formula. However, this optimization must also account for the ability to compensate for misalignments caused by tooth deformation and assembly errors. In addition to noise emission calculations, the optimization includes the $K_{H\beta}$ factor, which considers load distribution F_m along the tooth width (Figure 13).

$$K_{H\beta} = \frac{\max(L_i)}{\frac{F_m}{n}}, \text{ where } F_m = \sum_{i=1}^{n} L_i \tag{44}$$

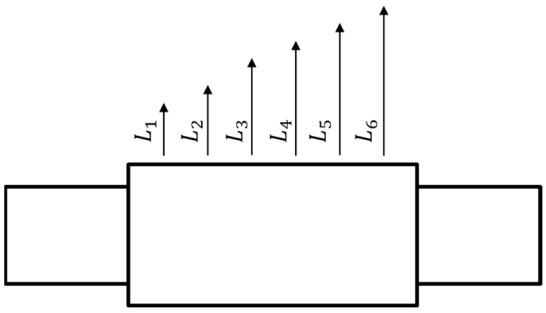

Figure 13. Load distribution along the tooth hub.

As a constraint of the optimization process, the limit $K_{H\beta} \leq 1.1$ is assumed to ensure a well-centered tooth contact, as shown in Figure 14.

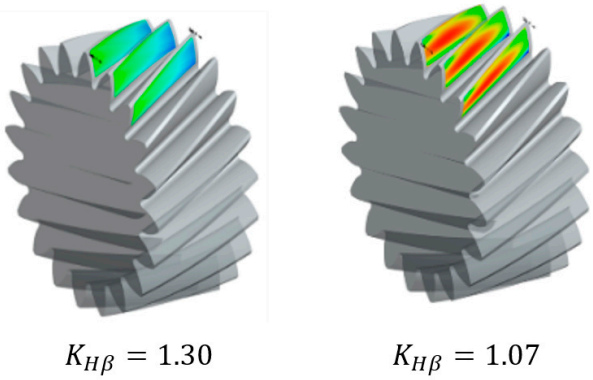

Figure 14. Comparison of a typical contact pressure distribution for different $K_{H\beta}$ values.

The objective functions are primarily aimed at minimizing noise emissions. Specifically, there are two:

- Peak–peak of static transmission error $(PPTE)$;
- Sound pressure level (SPL).

In Figure 15, all the variables included in the optimization process are shown in a flowchart.

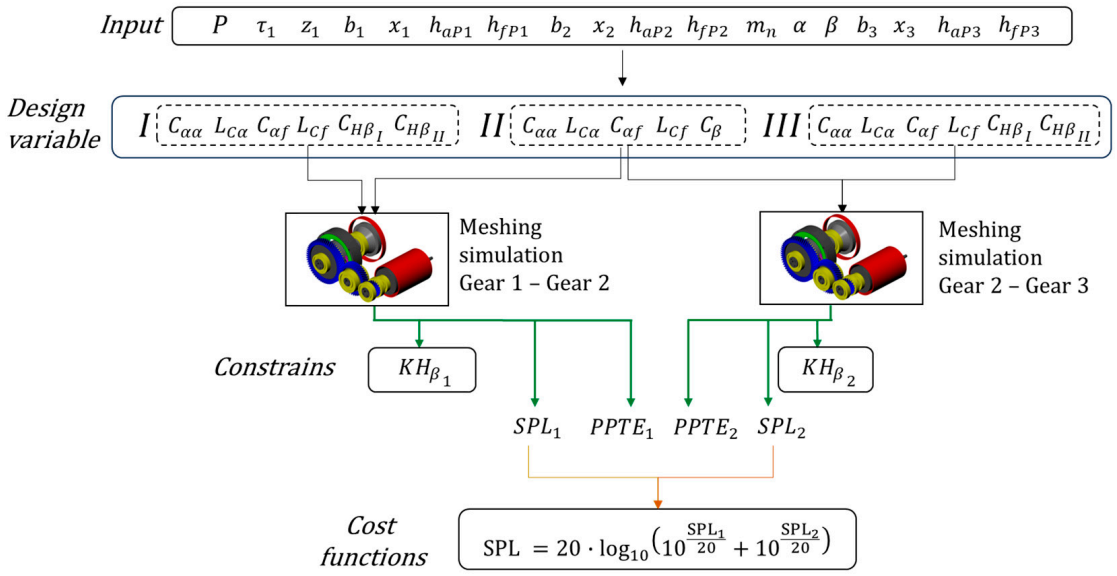

Figure 15. Flowchart of the micro-geometry optimization process.

7. Case Study Description and Results

The chosen case study for discussing the optimization methodology is an electric axle designed for a high-performance vehicle, shown in Figure 16. The considered configuration includes two equal electric motors, each dedicated to one half-shaft and to one wheel. The two sides of the axle are symmetric, and assuming their identical behavior, the analysis is conducted by considering only one side of the axle. The electrical power is converted into mechanical power through a two-stage helical gear reducer and a planetary gear set.

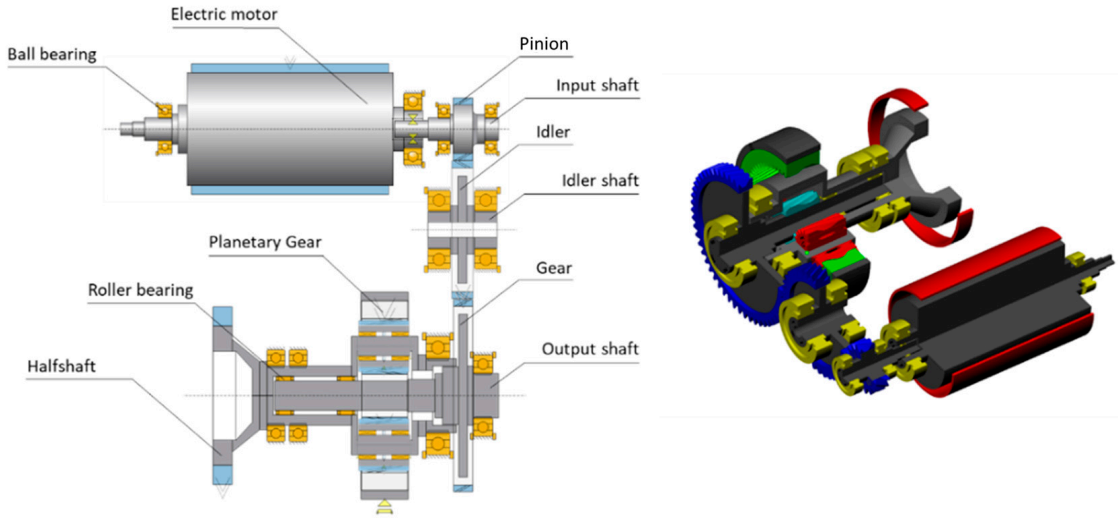

Figure 16. E-axle layout of a single wheel. On the left, a cross-section with nomenclature is depicted. On the right, a rendered isometric view is shown.

The optimization process is applied to the first and second reduction stage using helical gears. For the planetary gears, optimization is not performed as their configuration more evenly distributes forces, reducing noise and vibrations. Multiple gears are in simultaneous contact during operation, which better distributes the load and contributes to quieter operation. Furthermore, the goal is not to increase the complexity of the calculation and

to propose a generic methodology to be applied for all types of gears. The e-axle model is showed in Figure 17 and consists of

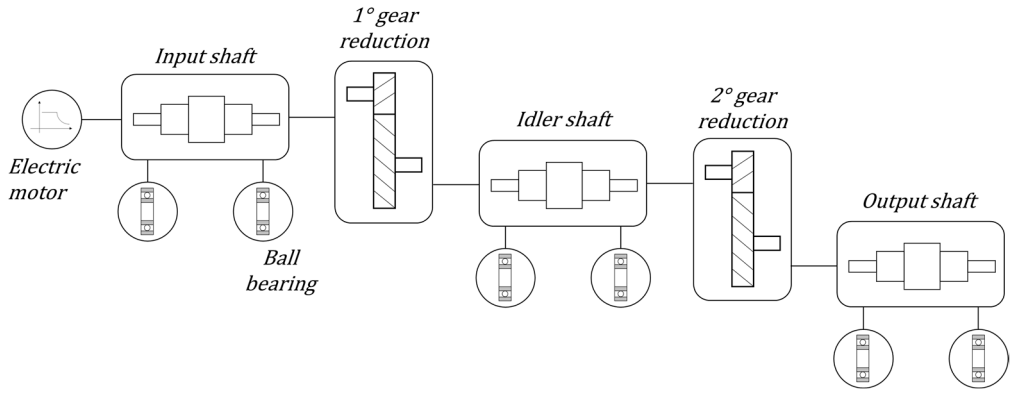

Figure 17. Schematic model of the e-axle of the case study.

- Four connection bodies: input shaft, idler shaft, output shaft, and ground;
- One driving element: electric motor;
- Two gear couplings;
- Six ball bearings.

The results of the optimization process for the case study are presented below. The initial population is generated using a design of experiments (DOE) with 200 cases, combining the variables according to the Latin hypercube sampling method. These initial solutions are calculated to generate the starting points for the calculations. The mutation and crossover process are used to generate 5000 samples, and these samples are used for each step in the new population. The computation time required to analyze each sample is about 3 s, allowing the optimizer to evaluate 5000 different solutions in 4 h using a Workstation equipped with an Intel Core i9 14900 processor and 64 Gb of Ram.

Reference values $\varepsilon_a^{ref} = 3$, $a^{ref} = 168$ mm, and $P_V^{ref} = 1.3$ kW are used. In Figure 18a, the optimization results for the contact ratio of the two gear pairs are presented. The results, primarily influenced by the second gear pair, indicate that solutions with a higher contact ratio are associated with increased cutting. Specifically, solutions achieving a higher contact ratio for the first gear pair tend to result in larger overall dimensions. Consequently, it is more advantageous to focus on maximizing the contact ratio of the second gear pair to minimize power loss. However, as shown in Figure 18b, increasing the contact ratio leads to higher power dissipation, as the greater number of teeth in contact intensifies the sliding between surfaces, resulting in increased friction and losses.

In Figure 19a, it is shown that solutions with a higher contact ratio for the first gear pair are associated with lower safety factors for bending and pitting, as the teeth tend to become thinner. Figure 19b illustrates the safety factors for the second gear pair, where similarly, higher safety factors are linked to a lower contact ratio. Although the results are less dispersed for the second gear pair, a similar trend is observed, with higher safety factors corresponding to a lower contact ratio. This demonstrates the effectiveness of the optimization process in selecting a configuration that meets the design constraints, achieving an optimal balance between reliability and transmission ratio.

Starting from an initial trial geometry, a new gear geometry is selected with the same input torque, center distance, and similar number of teeth for availability needs. A different transmission ratio is used because we are comparing two e-axles with a different target speed for output shaft. The new geometry is chosen to have a higher contact ratio (Table 7 and Figure 20), strictly correlated to the noise emission, and similar power loss with respect to the reference geometry. This is possible with better load distribution between the teeth,

leading to a reduction in the variation in mesh stiffness, which is a source of noise emission. Table 7 presents a summary of the calculated geometries.

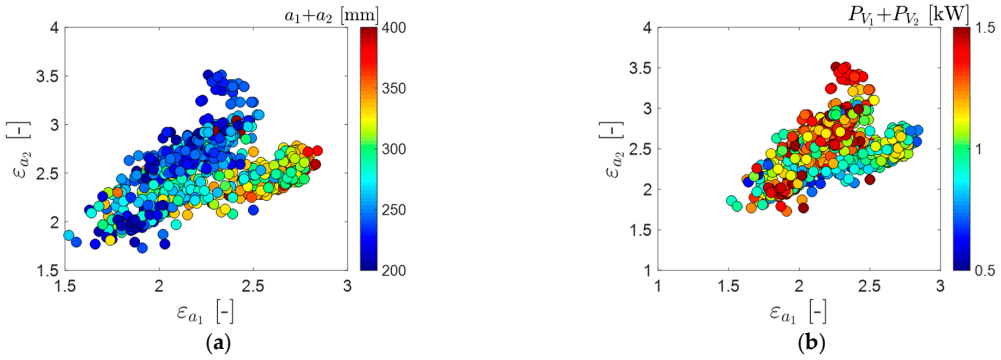

Figure 18. (**a**) Results of contact ratio relative to center-to-center distance. (**b**) Results of contact ratio relative to power loss.

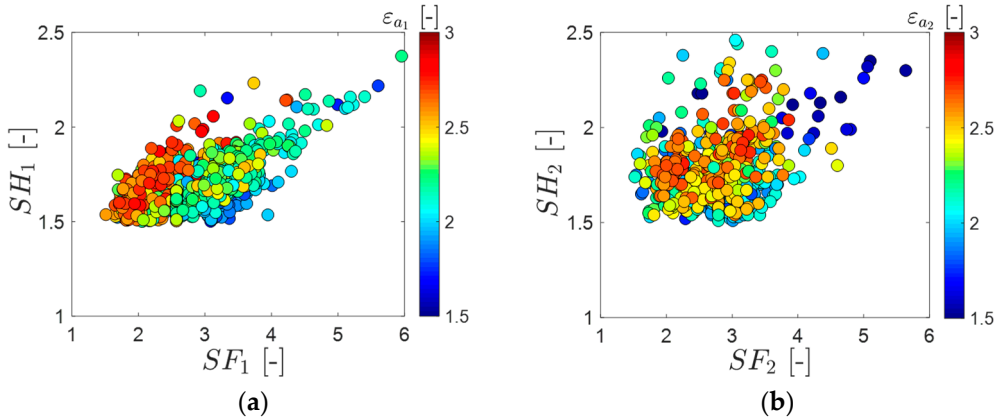

Figure 19. Results of bending and pitting safety factors relative to the contact ratio: (**a**) first gear pair; (**b**) second gear pair.

Table 7. Comparison of macro-geometry between the non-optimized configuration and the optimized configuration with a higher contact ratio.

			Initial/Reference			**Optimized**		
			Pinion	***Idler***	***Output***	***Pinon***	***Idler***	***Output***
Torque	M	[Nm]	85	201	292	85	183	251
Speed	ω	[rpm]	10,000	4210	2909	10,000	4651	3389
Normal module	m_n	[mm]	2.0	2.0	2.0	1.8	1.8	1.8
Pressure angle	α	[°]	20	20	20	20	20	20
Helix angle	β	[°]	28.5	28.5	28.5	28.5	28.5	28.5
Addendum factor	h_{aP}	[mm]	2.869	2.889	2.868	1.20	1.50	1.50
Dedendum factor	h_{fP}	[mm]	2.431	2.811	2.932	1.80	1.80	1.80
Number of teeth	z	[-]	16	38	55	20	43	59
Correction factor	x	[-]	0.407	0.150	0.092	0.390	0	−0.359
Face width	b	[mm]	13	14	13	20	18	19.9
Center distance	a	[mm]	62.5	106.3		65.2	103.8	
Transverse contact ratio	ε_a	[-]	1.345	1.661		1.692	2.123	
Power loss	P_{VZ}	[kW]	0.85	0.45		0.80	0.50	

For the micro-geometry optimization, an initial population is generated using the DOE approach with a Latin hypercube distribution, considering 50 samples. In this case, a smaller number of samples is employed due to the increased computational time required for each

iteration. Each iteration is solved in 15 s. This increase occurs because both tooth contact and shaft deformation are calculated during this phase. Therefore, for the mutation and crossover process, in which 5000 samples are used, and these samples are applied at each step in the new population, the total computation time is 21 h. The algorithm is applied to the geometry of gears with a higher contact ratio, under identical torque and speed conditions, to achieve performance enhancements. The optimization of the tooth profile is carried out to further improve the acoustic performance of the transmission system. Figure 21 presents the optimization results in terms of the acoustic pressure level and the peak-to-peak transmission error for both gear pairs. The optimization algorithm finds the set of solutions that minimize the acoustic pressure level and the peak-to-peak transmission error while satisfying the imposed constraints. The feasible solution set is illustrated, emphasizing the relationship between the sound pressure level and the transmission error for both gear pairs. Additionally, the Pareto front is identified, representing the set of solutions where it is impossible to further reduce the acoustic pressure level without increasing the transmission error, and vice versa. The results in Figure 21 also show that, although the relationship between PPTE and SPL is preserved, the solution set converges towards the Pareto front. This is because Equation (A19) depends not only on PPTE but also on other design parameters. As a result, it is not possible to reduce the PPTE of one gear stage without negatively affecting the other. The figure shows how the reduction in acoustic emission is directly correlated with the reduction in transmission error. The optimizer reaches the Pareto front, representing the set of solutions where further reduction in acoustic pressure level is impossible without increasing transmission error, and vice versa. The two star symbols represent the initial and final configurations of the optimizer. It is evident that the optimizer succeeded in improving the acoustic emission starting from the initial solution.

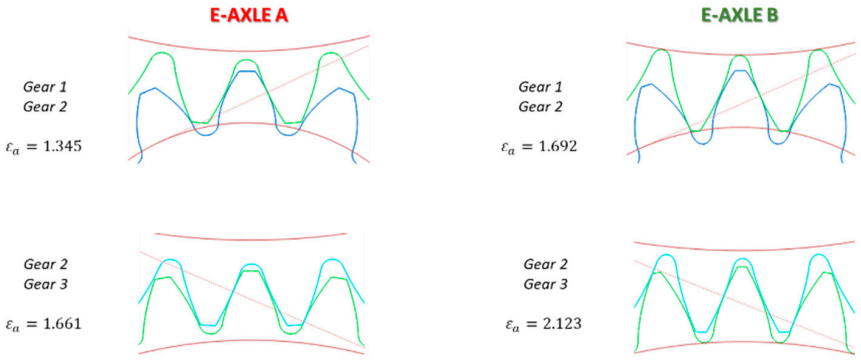

Figure 20. Comparison of tooth geometry with different contact ratio.

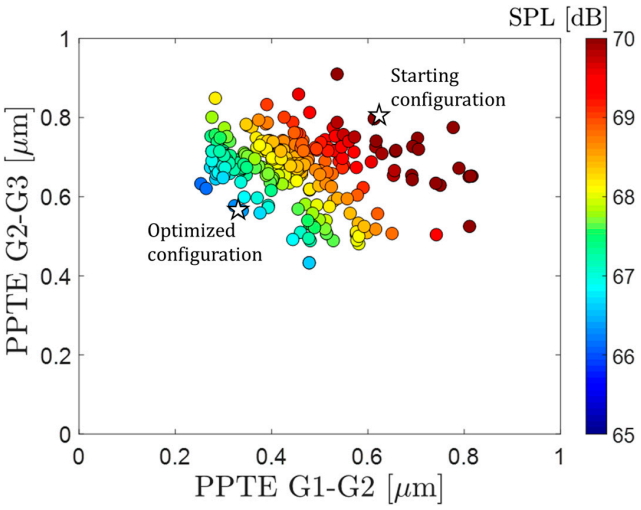

Figure 21. Micro-geometry optimization results.

8. Experimental Results, Verification, and Discussion

To verify the calculation method, two e-axle geometries were tested: the first one with non-optimized parameters and the other one designed and manufactured after the optimization process. For both geometries, noise measurements were conducted using an analog PCB. microphone model HT378B02 by PCB Technologies Ltd. (Ocean Township, NJ, USA) with the following specifications:

- Nominal diameter: ½;
- Frequency response characteristic: free-field;
- Frequency range: (±2 dB) 3.5 to 20,000 Hz (3.5 to 20,000 Hz);
- Dynamic range: 138.5 dB re 20 µPa.

The test was conducted in an anechoic chamber. Specifically, an electric axle consisting of independent electric machines was used. Each electric machine applies a maximum torque of 45 Nm at 1000 rpm, with a maximum speed of 15,000 rpm. The electric axle is connected to the test rig via two half-shafts, each linked to a brake. Additionally, torque transducers are employed to measure the torque applied to the brake. The gears used are those described in Table 7. Both the initial configuration and the optimized one were tested to validate the computational method. The tested maneuver involved ramping up from 10,000 rpm to 15,000 rpm. The microphone is positioned 10 mm from the e-axle, located at the midpoint of the first two reduction stages, as shown in Figure 22. No additional microphones are present in the test setup, as the computational model does not account for dynamic effects such as wave reflections.

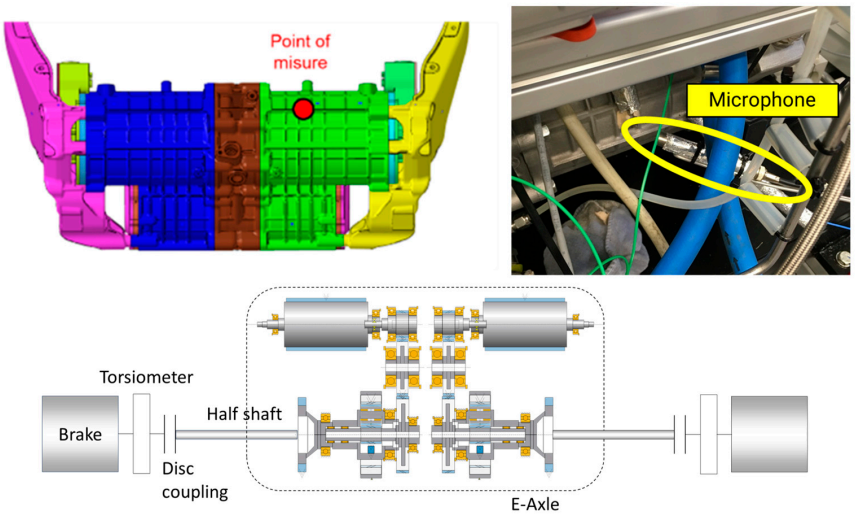

Figure 22. Experimental setup details. Top left: schematic representation of the microphone position; top right: image of the microphone position in the experimental setup; bottom: configuration of the overall transmission system.

To account for the difference in microphone position between Masuda's model (1 m from the gears) and the experimental setup (1.4 cm from the first reduction stage and 2.1 cm from the second stage), a correction is applied to the original formula. Specifically, an additional contribution is added:

$$SPL_{\text{Tot}} = SPL_{\text{masuda}} + \log\left(\frac{d_1}{d_2}\right) \tag{45}$$

where

d_1 is the distance between the center of the gear and the microphone in Masuda's model;
d_2 is the distance between the center of the gear and the microphone in the experiment.

Figure 23 illustrates the SPL for two distinct electric axle configurations. The red curve represents the baseline, i.e., the non-optimized configuration, while the green curve corresponds to the configuration obtained after the optimization process. Since the adopted method does not account for the model's nonlinear characteristics, the analysis is limited to the ramp-up phase in both the experimental data and the simulation. Both experimental and simulation results show a reduction in sound pressure level between the optimized and non-optimized configurations. The simulations capture this effect, confirming the effectiveness of the calculation method. However, the model does not consider dynamic effects such as housing and shaft resonances, which limits its ability to capture variations in the amplitude of the sound pressure level. The comparison with experimental measurements supports the notion that the improvements predicted by the calculations are consistent with the experimental results. Additionally, it is observed that while Masuda's method accurately captures the average acoustic pressure levels, it does not adequately represent the system's dynamic behavior.

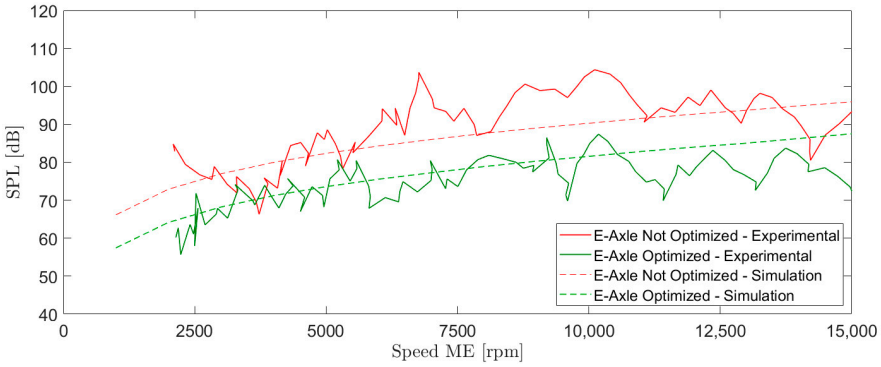

Figure 23. Comparison of experimental measurements and simulated noise emissions.

The observed improvement is primarily driven by the reduction in transmission error (Figure 24), which, as highlighted in the literature, is a key factor influencing noise transmission. The results suggest that the main cause of the reduction in acoustic emission between the two configurations is linked to the reduction in peak-to-peak transmission error. This reduction is achieved through both the optimization of microgeometry, which increases the contact ratio and reduces variations in meshing stiffness, and the improvement of profile geometry. However, this modeling approach does not fully address transmission error, as it does not account for dynamic effects and system resonances that could amplify it. A more comprehensive approach would involve a higher computational burden, making it more suitable for detailed calculations. The methodology presented in this article is intended to provide design guidelines during the early stages of development, with detailed calculations reserved for the phases leading up to production implementation.

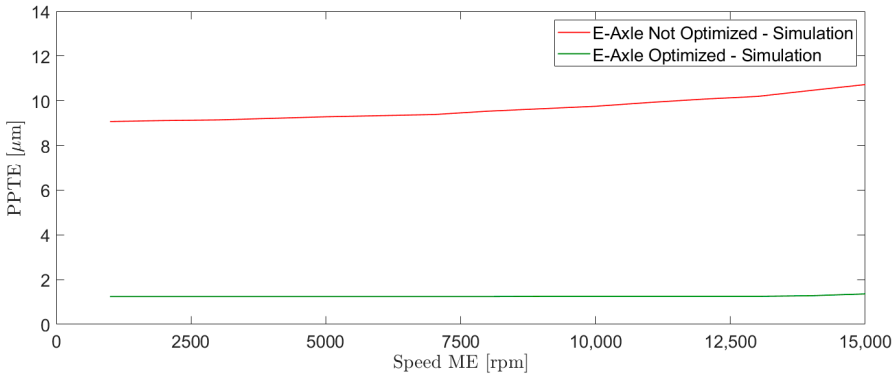

Figure 24. Comparison of peak-to-peak transmission error for starting and optimized design.

9. Conclusions

This work presents a two-stage optimization strategy aimed at enhancing the acoustic performance of automotive electric axles through the refinement of gear macro- and micro-geometry. The optimization framework is based on the NSGA-II evolutionary algorithm and employs reduced-order lumped parameter models to describe the elastic behavior of key transmission components, including electric motors, ball bearings, shafts, and gear pairs. This modeling approach ensures a favorable trade-off between computational efficiency and predictive accuracy.

The methodology was applied to an industrial case study and subsequently validated through experimental measurements conducted on two electric axle prototypes. The optimized configurations led to a significant reduction in noise emissions, primarily attributed to the minimization of transmission error. The consistency observed between numerical predictions and experimental results confirms the validity of the modeling assumptions and simplifications adopted in the formulation of the lumped parameter models.

Minor deviations between simulation and test data were observed and are mainly due to the absence of dynamic amplification effects in the current model formulation. These discrepancies highlight the potential benefits of extending the models to include inertial contributions and nonlinearities in the dynamic transmission error, thereby improving the fidelity of the simulation results under dynamic operating conditions.

The proposed optimization methodology not only accelerates the convergence toward acoustically optimal solutions but also ensures compliance with manufacturability constraints. Given its modular structure and computational efficiency, the approach can be generalized and applied to a broad class of mechanical transmission systems, supporting the development of low-noise, high-performance driveline architectures. Future work on this topic should include the investigation of the coupling effect of the noise/vibration of the motor with the gearbox and the effect of bearing typologies and dimensions.

Author Contributions: Conceptualization, P.P.V. and M.C.; methodology, L.C. and P.P.V.; software, L.C.; validation, L.C. and M.C. writing—original draft preparation, L.C.; writing—review and editing, M.C. and P.P.V.; supervision, P.P.V.; funding acquisition, P.P.V. All authors have read and agreed to the published version of the manuscript.

Funding: This research was funded by the Italian Ministry for University and Research, PRIN 2020 project "Innovative Contact Based multibody models for noise and vibration prediction in high-performance gears" grant number 202022Y4N5. CUP E85F22000220006.

Data Availability Statement: Data is contained within the article.

Acknowledgments: The paper is dedicated to the memory of Ettore Pennestrì, friend, mentor, and never-ending source of inspiration in the field of machines, transmissions, and mechanisms.

Conflicts of Interest: The authors declare no conflicts of interest. The funders had no role in the design of the study; in the collection, analyses, or interpretation of data; in the writing of the manuscript; or in the decision to publish the results.

Appendix A

Appendix A.1

The nominal contact stress is calculated as

$$\sigma_{H0} = Z_H \cdot Z_E \cdot Z_\varepsilon \cdot Z_\beta \cdot \sqrt{\frac{F_t}{d_p \cdot b} \cdot \frac{\tau + 1}{\tau}} \tag{A1}$$

where

Z_H is the zone factor, which takes into account the influence of flank curvatures at the pitch point on Hertzian pressure;
Z_E is the elasticity factor, which takes into account specific properties of the material, moduli of elasticity E, and Poisson's ratios ν;
Z_ε is the contact ratio factor, which takes into account the influence of the effective length of the lines of contact;
Z_β is the helix angle factor, which considers the influence of the helix angle, such as the variation in the load along the lines of contact;
τ is the contact ratio of the single stage.

Further details on the computation of Z_H, Z_E, Z_ε, and Z_β factors can be found in [41].

To account for load variations relative to the nominal load, the following factors are also introduced:

$$\sigma_H = \sigma_{H0} \cdot Z_{BD} \cdot \sqrt{K_A \cdot K_V \cdot K_{H\beta} \cdot K_{H\alpha}} \quad \text{(A2)}$$

where

Z_{BD} is the single-pair tooth contact factor that converts contact stress at the pitch point to contact stress at the inner point;
K_A is the application factor, which takes into account load increments due to externally influenced variations in input or output torque;
K_V is the dynamic factor, which takes into account load increments due to internal dynamic effects;
$K_{H\beta}$ is the face load factor for contact stress, which takes into account the effect of an uneven load distribution over the face width on the contact stress;
$K_{H\alpha}$ is the transverse load factor for contact stress, which considers uneven load distribution in the transverse direction, resulting, for example, from pitch deviations.

Details on how to evaluate the Z_{BD}, K_A, K_V and $K_{H\alpha}$ factors can be found in [47]. ISO 6336-2 [48], method B defines the allowable contact stress as the product between the following coefficients:

$$\sigma_{HP} = \frac{\sigma_{H,\lim}}{S_{H,\min}} \cdot Z_L \cdot Z_V \cdot Z_R \cdot Z_W \cdot Z_X \cdot Z_{NT} \quad \text{(A3)}$$

where

$S_{H,min}$ is the minimum required safety factor for contact stress;
$\sigma_{H,lim}$ is the stress limit that is computed according to [49], as a function of the material quality;
Z_L is the lubricant factor, which accounts for the influence of lubricant viscosity on the effect of the lubricant film;
Z_V is the velocity factor, which accounts for the influence of pitch line velocity on the effect of the lubricant film;
Z_R is the roughness factor, which accounts for the influence of surface roughness of the flanks on the effect of the lubricant film;
Z_W is the work hardening factor, which accounts for the effect of meshing with a surface-hardened or similarly hard mating gear;
Z_X is the size factor relevant to contact stress, which considers the influence of tooth dimensions on the permissible contact stress;
Z_{NT} is the life factor for test gears for contact stress. It considers the higher load capacity for a limited number of load cycles.

The limit contact stress is the product between the minimum required safety factor and the allowable contact stress:

$$\sigma_{HG} = \sigma_{HP} \cdot S_{H,\min} \quad \text{(A4)}$$

Once σ_{HP} and σ_H are known, their ratio provides the pitting safety factor:

$$SH = \frac{\sigma_{HG}}{\sigma_H} \tag{A5}$$

Appendix A.2

The nominal tooth root stress is evaluated as

$$\sigma_{F0} = \frac{F_t}{b \cdot m_n} \cdot Y_F \cdot Y_S \cdot Y_\beta \cdot Y_B \cdot Y_{DT} \tag{A6}$$

where

Y_F is the form factor, which takes into account the influence on nominal tooth root stress of the tooth form, with load applied at the outer point of single pair tooth contact;
Y_S is the stress concentration factor, which is used to convert the nominal tooth root stress to local tooth root stress. It takes into account the stress-amplifying effect of section change at the filet radius at tooth root;
Y_β is the helix angle factor, which compensates for the fact that the bending moment intensity at the tooth root of helical gears is—as a consequence of the oblique lines of contact—less than the corresponding value for the virtual spur gears used as the bases for calculation;
Y_B is the rim thickness factor, which adjusts the calculated tooth root stress for thin rimmed gears;
Y_{DT} is the deep tooth factor, which adjusts the calculated tooth root stress for high precision gears with a high contact ratio ε_α.

To take into account the variations in load, multiplication factors are considered:

$$\sigma_F = \sigma_{F0} \cdot K_A \cdot K_V \cdot K_{F\beta} \cdot K_{F\alpha} \tag{A7}$$

where

σ_{F0} is the nominal tooth root stress, which is the maximum local principal stress produced at the tooth root when a gear pair is loaded by the static nominal torque;
K_A is the application factor, which takes into account load increments due to externally influenced variations in input or output torque;
K_V is the dynamic factor, which takes into account load increments due to internal dynamic effects;
$K_{F\beta}$ is the face load factor for tooth root stress, which considers the effect of an uneven load distribution over the face width on the stresses at the tooth root. The uneven load distribution is due to mesh misalignment caused by inaccuracies in manufacture, elastic deformations and so on;
$K_{F\alpha}$ is the transverse load factor for tooth root stress, which considers uneven load distribution in the transverse direction.

Details on how to evaluate the factors K_A, K_V, $K_{F\beta}$, and $K_{F\alpha}$ can be found in [47]. In the following sections, a more detailed explanation of σ_{F0} is given. ISO 6336-3 [38], method B, defines the allowable tooth root stress as the product between the following coefficients:

$$\sigma_{FP} = \frac{\sigma_{F,\mathrm{lim}}}{SF_{\mathrm{min}}} \cdot Y_{ST} \cdot Y_M \cdot Y_{\delta \mathrm{rel\ T}} \cdot Y_{R\mathrm{rel\ T}} \cdot Y_X \cdot Y_{NT} \tag{A8}$$

where

SF_{min} is the minimum required safety factor for tooth root stress;

$\sigma_{F,lim}$ is the limit stress and the value can be retrieved from [49], as a function of the material quality and the core hardness;
Y_{ST} is the stress correction factor, depending on the standard reference test gear used to characterize the material;
Y_M is the alternating bending factor, whose value depends on the gear working conditions [50];
$Y_{\delta rel\ T}$ is the relative notch sensitivity factor. It is the ratio between the notch sensitivity factor of the gear of interest and the standard test gear factor; it does not show any significant dependence with respect to the number of cycles;
$Y_{Rrel\ T}$ is the relative surface factor. It is the ratio between the surface roughness factor of tooth root filets of the gear of interest and the toot root filet factor of the reference test gear; it does not show any significant dependence with respect to the number of cycles;
Y_X is the size factor relevant to tooth strength, which is used to consider the influence of tooth dimensions on tooth bending strength. Its value depends on the normal module m_n and on the material;
Y_{NT} is the life factor for tooth root stress. It considers the higher load capacity for a limited number of load cycles. In practice, this is the parameter which makes the permissible stress dependent on the number of cycles.

The limit root stress is the product between the minimum required safety factor and the allowable tooth root stress:

$$\sigma_{FG} = \sigma_{FP} \cdot SF_{\min} \tag{A9}$$

Once σ_{FG} and σ_F are known, their ratio provides the bending safety factor:

$$SF = \frac{\sigma_{FG}}{\sigma_F} \tag{A10}$$

Appendix A.3

The zero-load gear system losses are determined without considering the distinction between splash and squeeze losses. The total hydraulic loss torque T_H of a gear stage is determined using the following:

$$T_H = C_{s_p} C_1 e^{C_2\left(\frac{v_t}{v_{t0}}\right)} \tag{A11}$$

where

$$C_{s_p} = \left(\frac{4h_{e,\max}}{3h_c}\right)^{1.5} \frac{2h_c}{l_h} \tag{A12}$$

$$C_1 = 0.063\left(\frac{h_{e1} + h_{e2}}{h_{e0}}\right) + 0.0128\left(\frac{b}{b_0}\right)^3 \tag{A13}$$

$$C_2 = \frac{h_{e1} + h_{e2}}{80\, h_{e0}} + 0.2 \tag{A14}$$

with h_{e1}, h_{e2} the tip circle immersion depth with oil level stationary, b the tooth width, $h_{e,max}$ the max tip circle immersion depth with oil level stationary, h_c the height of point of contact above the lowest point of the immersion gear, $h_{e0} = 10$ mm, $b_0 = 10$ mm, $v_{t0} = 10$ m/s. l_h is the hydraulic length defined as

$$l_h = \frac{4A_G}{U_m} \tag{A15}$$

where A_G is the cross-sectional area of the flow (how much space the lubricant has to flow) and U_m is the wetted perimeter (how much of the fluid is in contact with solid surfaces).

The zero-load power loss can be calculated by multiplying the zero-load torque with the angular velocity of the gear wheel of the stage. The total zero-load power loss is the

sum of the zero-load power losses of all stage N_{stage}, considering $T_{H,i}$ is the loss torque and n_i the rotational speed of the gear wheel of the gear stage i:

$$P_{\mathrm{VZ0}} = \sum_{i=1}^{N_{\mathrm{stage}}} T_{H,i} \frac{n_i}{30} \tag{A16}$$

The load dependent gear loss is calculated according to Coulomb law:

$$P_{\mathrm{VZP}} = F_n(x) \cdot \mu(x) \cdot v_g(x) \tag{A17}$$

where F_n is the tooth normal force, μ the coefficient of friction, and v_g the sliding speed at each point x of the path of contact. The coefficient of friction is approximated in the following way:

$$\mu_{mz} = 0.048 \left(\frac{F}{b} \cdot \frac{1}{\nu_{oil} \rho_{oil}} \right)^{0.2} \eta_{oil}^{0.05} Ra^{0.25} X_L \tag{A18}$$

where $Ra = 0.5\ (Ra_1 + Ra_2)$ is the average of the arithmetic roughness $Ra_{1/2}$ of the pinion and gear wheel, and the lubricant factor X_L (see more details in [40]), ν_{oil} is the kinematic viscosity, ρ_{oil} the oil density, and η_{oil} the dynamic viscosity.

The bearing loss torque, T_{VL}, is split into zero-load, T_{VL0}, and load-dependent, T_{VLP1}, parts. In the case of axially loaded cylindrical roller bearings and axially loaded needle roller bearings, an additional loss term, T_{VLP2}, occurs, which is dependent on the magnitude of the end thrust. These components are calculated separately and then added together to give the following for the total loss torque:

$$T_{\mathrm{VL}} = T_{\mathrm{VL0}} + T_{\mathrm{VLP1}} + T_{\mathrm{VLP2}} \tag{A19}$$

The zero-load component depends on the bearing design, the type of lubrication, the viscosity of the lubricant, and the bearing speed, with

$$T_{\mathrm{VL0}} = \begin{cases} 1.6 \cdot 10^8 f_0 d_m^3, & \nu_{\mathrm{oil}} \cdot n < 2000 \\ 10^{10} (\nu_{\mathrm{oil}} \cdot n)^{\frac{2}{3}} f_0 d_m^3, & \nu_{\mathrm{oil}} \cdot n \geq 2000 \end{cases} \tag{A20}$$

where f_0 depends on the bearing type and bearing lubrification (see more details in [40]), n is the bearing speed, and d_m the mean bearing diameter. For calculation of the load-dependent bearing loss torques, T_{VLP1} and T_{VLP2}, the following relationship

$$T_{VLP1} = f_1 {P_1}^a d_m^b 10^3 \tag{A21}$$

$$T_{VLP2} = f_2 F_a d_m 10^3 \tag{A22}$$

where f_1, f_2 are the bearing coefficient (see details in [40]), P_1 is the equivalent bearing load, and F_a is the thrust load. From the calculated loss torque of each bearing $T_{VL0,i}$, $T_{VLP,i}$, it is possible to calculate the total bearing power loss of $N_{bearing}$ as follows:

$$P_{VL0} + P_{VLP} = \sum_{i=1}^{N_{\mathrm{bearing}}} T_{VL0,i} \frac{n_i}{30} + \sum_{i=1}^{N_{\mathrm{stage}}} T_{VLP,i} \frac{n_i}{30} \tag{A23}$$

For non-contacting seals, it can be assumed as an approximation that no contribution to power loss occurs. The power loss for shaft seals is calculated according to [40] as

$$P_{\mathrm{VD}} = 7.69 \cdot 10^6 d_{\mathrm{sh}}^2 n$$

References

1. Gissel, M.; Nielsen, A.F. Influence of gear tooth geometry on the noise and vibration of gears. *J. Sound Vib.* **2000**, *238*, 381–395.
2. Rosso, C.; Bruzzone, F.; Maggi, T.; Marcellini, C. *Influence of Micro Geometry Modification on Gear Dynamics*; SAE Technical Paper 2020-01-1323; SAE International: Warrendale, PA, USA, 2020.
3. Stroud, I.R.; Hartley, P.F. The effect of gear surface finish on noise and vibration performance. *Proc. Inst. Mech. Eng. Part C J. Mech. Eng. Sci.* **2001**, *2015*, 1261–1270.
4. Choi, W.; Lee, C.H. Effect of manufacturing errors on the vibration characteristics of gears. *J. Mech. Des.* **2018**, *32*, 2107–2114.
5. Kahraman, A.; Blankenship, G.W. Effect of Involute Contact Ratio on Spur Gear Dynamics. *J. Mech. Des.* **1999**, *121*, 112–118. [CrossRef]
6. Sato, T.; Umezawa, K.; Ishikawa, J. Effects of Contact Ratio and Profile Correction on Gear Rotational Vibration. *Bull. JSME* **1983**, *26*, 2010–2016. [CrossRef]
7. Staph, H.E. A Parametric Analysis of High-Contact-Ratio Spur Gears. *A S L E Trans.* **1976**, *19*, 201–215. [CrossRef]
8. Cornell, R.W.; Westervelt, W.W. Dynamic Tooth Loads and Stressing for High Contact Ratio Spur Gears. *J. Mech. Des.* **1978**, *100*, 69–76. [CrossRef]
9. Anderson, N.E.; Loewenthal, S.H. Efficiency of Nonstandard and High Contact Ratio Involute Spur Gears. *J. Mech. Trans. Autom.* **1986**, *108*, 119–126. [CrossRef]
10. Ozguven, H.; Houser, D. Mathematical models used in gear dynamics—A review. *J. Sound Vib.* **1988**, *121*, 383–411. [CrossRef]
11. Chang, L.; Liu, G.; Wu, L. A robust model for determining the mesh stiffness of cylindrical gears. *Mech. Mach. Theory* **2015**, *87*, 93–114. [CrossRef]
12. Kahraman, A.; Blankenship, G. Gear dynamics experiments, Part-I: Characterization of forced response. In Proceedings of the ASME 6th Power Transmission and Gearing Conference Phoenix, Phoenix, AZ, USA, 13–16 September 1996.
13. Cirelli, M.; Valentini, P.P.; Pennestrì, E. A study of the non-linear dynamic response of spur gear using a multibody contact based model with flexible teeth. *J. Sound Vib.* **2019**, *445*, 148–167. [CrossRef]
14. Kahraman, A.; Blankenship, G.W. Effect of Involute Tip Relief on Dynamic Response of Spur Gear Pairs. *J. Mech. Des.* **1999**, *121*, 313–315. [CrossRef]
15. Cirelli, M.; Giannini, O.; Valentini, P.P.; Pennestrì, E. Influence of tip relief in spur gears dynamic using multibody models with movable teeth. *Mech. Mach. Theory* **2020**, *152*, 103948. [CrossRef]
16. Autiero, M.; Paoli, G.; Cirelli, M.; Valentini, P.P. The effect of different profile modifications on the static and dynamic transmission error of spur gears. *Mech. Mach. Theory* **2024**, *201*, 105752. [CrossRef]
17. Munro, R.G.; Palmer, D.; Morrish, L. An experimental method to measure gear tooth stiffness throughout and beyond the path of contact. *Proc. Inst. Mech. Eng. Part C J. Mech. Eng. Sci.* **2001**, *215*, 793–803. [CrossRef]
18. Palermo, A.; Britte, L.; Janssens, K.; Mundo, D.; Desmet, W. The measurement of Gear Transmission Error as an NVH indicator: Theoretical discussion and industrial application via low-cost digital encoders to an all-electric vehicle gearbox. *Mech. Syst. Signal Process.* **2018**, *110*, 368–389. [CrossRef]
19. Kahraman, A.; Tamminana, V.; Vijayakar, S. A Study of the Relationship Between the Dynamic Factors and the Dynamic Transmission Error of Spur Gear Pairs. *J. Mech. Des.* **2007**, *129*, 75–84.
20. Cirelli, M.; Autiero, M.; Belfiore, N.P.; Paoli, G.; Pennestrì, E.; Valentini, P.P. Review and comparison of empirical friction coefficient formulation for multibody dynamics of lubricated slotted joints. *Multibody Syst. Dyn.* **2024**, *63*, 83–104. [CrossRef]
21. Autiero, M.; Cera, M.; Cirelli, M.; Pennestrì, E.; Valentini, P.P. Review with Analytical-Numerical Comparison of Contact Force Models for Slotted Joints in Machines. *Machines* **2022**, *10*, 966. [CrossRef]
22. Lohmann, C.; Walkowiak, M.; Tenberge, P. Optimal modifications on helical gears for good load distribution and minimal wear. In Proceedings of the International Gear Conference 2014, Lyon, France, 26–28 August 2014.
23. Autiero, M.; Cirelli, M.; Paoli, G.; Valentini, P.P. A Data-Driven Approach to Estimate the Power Loss and Thermal Behaviour of Cylindrical Gearboxes under Transient Operating Conditions. *Lubricants* **2023**, *11*, 303. [CrossRef]
24. Abdelounis, H.B.; Bot, A.L.; Liaudet, J.P.; Zahouani, H. An experimental study on roughness noise of dry rough flat surfaces. *Wear* **2010**, *268*, 335–345. [CrossRef]
25. Chung, W.-J.; Park, Y.-J.; Choi, C.; Kim, S.-C. Effects of manufacturing errors of gear macro-geometry on gear performance. *Sci. Rep.* **2023**, *13*, 50. [CrossRef]
26. Geradts, P.; Brecher, C.; Löpenhaus, C.; Kasten, M. Reduction of the tonality of gear noise by application of topography scattering. *Appl. Acoust.* **2019**, *148*, 344–359. [CrossRef]
27. Ben Younes, E.; Changenet, C.; Bruyère, J.; Rigaud, E.; Perret-Liaudet, J. Multi-objective optimization of gear unit design to improve efficiency and transmission error. *Mech. Mach. Theory* **2022**, *167*, 104499. [CrossRef]
28. Choi, C.; Ahn, H.; Yu, J.; Han, J.-S.; Kim, S.-C.; Park, Y.-J. Optimization of gear macro-geometry for reducing gear whine noise in agricultural tractor transmission. *Comput. Electron. Agric.* **2021**, *188*, 106358. [CrossRef]

29. Kim, S.-C.; Moon, S.-G.; Sohn, J.-H.; Park, Y.-J.; Choi, C.-H.; Lee, G.-H. Macro geometry optimization of a helical gear pair for mass, efficiency, and transmission error. *Mech. Mach. Theory* **2020**, *144*, 103634. [CrossRef]
30. Choi, C.; Ahn, H.; Park, Y.-J.; Lee, G.-H.; Kim, S.-C. Influence of gear tooth addendum and dedendum on the helical gear optimization considering mass, efficiency, and transmission error. *Mech. Mach. Theory* **2021**, *166*, 104476. [CrossRef]
31. Korta, J.A.; Mundo, D. Multi-objective micro-geometry optimization of gear tooth supported by response surface methodology. *Mech. Mach. Theory* **2017**, *109*, 278–295. [CrossRef]
32. Garambois, P.; Perret-Liaudet, J.; Rigaud, E. NVH robust optimization of gear macro and microgeometries using an efficient tooth contact model. *Mech. Mach. Theory* **2017**, *117*, 78–95. [CrossRef]
33. Mohammed, O.D.; Bhat, A.D.; Falk, P. Robust multi-objective optimization of gear microgeometry design. *Simul. Model. Pract. Theory* **2022**, *119*, 102593. [CrossRef]
34. Marafona, J.D.; Carneiro, G.N.; Marques, P.M.; Martins, R.C.; António, C.C.; Seabra, J.H. Gear design optimization: Stiffness versus dynamics. *Mech. Mach. Theory* **2024**, *191*, 105503. [CrossRef]
35. Yang, J.-X.; Chen, Z.-Y.; Shi, W.-K.; Yang, H.-B.; Liu, J.; Yuan, R.-F.; Zhao, Y.-Y.; Dong, Y.-H. Robust modification optimization for helical gear mounting errors based on contact ratio. *Measurement* **2024**, *237*, 115196. [CrossRef]
36. Dixit, Y.; Kulkarni, M.S. Multi-objective optimization with solution ranking for design of spur gear pair considering multiple failure modes. *Tribol. Int.* **2023**, *180*, 108284. [CrossRef]
37. Masuda, T.; Abe, T.; Hattori, K. Prediction Method of Gear Noise Considering the Influence of the Tooth Flank Finishing Method. *J. Vib. Acoust.* **1986**, *108*, 95–100. [CrossRef]
38. *ISO 16281*; Rolling Bearings–Methods for Calculating the Modified Reference Rating Life for. International Organization for Standardization: Geneva, Switzerland, 2025.
39. Weber, C. *The Deformations of Loaded Gears and the Effect on Their Load-Carrying Capacity*; Report No.3; British Department of Scientific and Industrial Research: London, UK, 1949.
40. Mengjiao, F.; Ma, H.; Zhanwei, L.; Wang, Q.; Wen, B. An improved analytical method for calculating time-varying mesh stiffness of helical gears. *Meccanica* **2017**, *53*, 1131–1145.
41. *ISO 6336-2*; Calculation of Surface Durability (Pitting). International Organization for Standardization: Geneva, Switzerland, 2007.
42. *ISO 6336-3*; Calculation of Tooth Bending Strength. International Organization for Standardization: Geneva, Switzerland, 2007.
43. *BS ISO/TR 14179-2:2001*; Gears-Thermal Capacity—Part 2: Thermal Load Carrying Capacity. British Standards Institution: London, UK, 2001.
44. Deb, K.; Pratap, A.; Agarwal, S.; Meyarivan, T. A fast and elitist multiobjective genetic algorithm: NSGA-II. *IEEE Trans. Evol. Comput.* **2002**, *6*, 182–197. [CrossRef]
45. Skrickij, V.; Bogdevičius, M. Vehicle gearbox dynamics: Centre distance influence on mesh stiffness and spur gear dynamics. *Transport* **2010**, *25*, 278–286. [CrossRef]
46. Luo, Y.; Baddour, N.; Liang, M. Effects of gear center distance variation on time varying mesh stiffness of a spur gear pair. *Eng. Fail. Anal.* **2017**, *75*, 37–53. [CrossRef]
47. *ISO 6336-1*; Basic Principles, Introduction and General Influence Factors. International Organization for Standardization: Geneva, Switzerland, 2007.
48. Del Pio, G.; Pennestrì, E.; Valentini, P.P. Kinematic and power-flow analysis of bevel gears planetary gear trains with gyroscopic complexity. *Mech. Mach. Theory* **2013**, *70*, 523–537. [CrossRef]
49. *ISO 6336-5*; Strength and Quality of Materials. International Organization for Standardization: Geneva, Switzerland, 2007.
50. Linke, H. *Stirnradverzahnung. Berechnung. Werkstoffe. Fertigung*; Carl Hanser-Verlag: München, Germany, 1996.